Gate-tunable cross-plane heat dissipation in single-layer transition metal dichalcogenides

Zhun-Yong Ong ●,* Gang Zhang, and Yong-Wei Zhang
Institute of High Performance Computing, A*STAR, Singapore 138632, Singapore

Linyou Cao
Department of Materials Science and Engineering, North Carolina State University, Raleigh, North Carolina 27695, USA;
Department of Physics, North Carolina State University, Raleigh, North Carolina 27695, USA;
and Department of Electrical and Computer Engineering, North Carolina State University, Raleigh, North Carolina 27695, USA

Efficient heat dissipation to the substrate is crucial for optimal device performance in nanoelectronics. We develop a theory of electronic thermal boundary conductance (TBC) mediated by remote phonon scattering for the single-layer transition metal dichalcogenide (TMD) semiconductors MoS_2 and WS_2, and model their electronic TBC with different dielectric substrates (SiO_2, HfO_2, and Al_2O_3). Our results indicate that the electronic TBC is strongly dependent on the electron density, suggesting that it can be modulated by the gate electrode in field-effect transistors, and this effect is most pronounced with Al_2O_3. Our work paves the way for the design of novel thermal devices with gate-tunable cross-plane heat-dissipative properties.

I. INTRODUCTION

Atomically thin two-dimensional (2D) transition metal dichalcogenide (TMD) semiconductors such as MoS_2 and WS_2 are promising alternative materials for the development of next-generation electronic devices [1,2]. At the nanoscale, the high power densities in these devices require efficient thermal management which is crucial for optimal device performance, with the thermal boundary conductance (TBC) of the 2D crystal-substrate interface playing a key role in the dissipation of excess Joule heat [3,4]. Therefore, clearer insights into the physical mechanisms underlying heat dissipation across the TMD-substrate interface may lead to the development of superior thermally aware TMD-based nanoelectronic designs, as well as novel applications in thermal energy harvesting or for channeling heat in ultracompact geometries.

One widely studied mechanism is the van der Waals coupling between the phonons of the 2D crystal and its substrate, which is believed to be the dominant component in the overall TBC [4]. The phononic TBC has been estimated using molecular dynamics (MD) simulations [5,6], elasticity theory [7–9], and density-functional-theory-based models [10]. Another mechanism of heat dissipation is the inelastic scattering of electrons in the 2D crystal by dipoles in the dielectric substrate, a phenomenon known widely as "remote phonon (RP)

scattering" or "surface optical phonon scattering" [11–14]. This phenomenon occurs for an insulating metal-oxide dielectric substrate (e.g., SiO_2) in which the oscillating dipoles originating from the bulk polar optical phonons create an evanescent surface electric field that scatters the electrons remotely. The associated electron-phonon coupling strength depends on the dielectric properties of the substrate and screening by the electrons in the TMD. In a high-κ dielectric substrate such as HfO_2 or Al_2O_3, inelastic RP scattering can be strong enough to cause substantial momentum relaxation of the TMD electrons [15]. In graphene [14,16], this mechanism is also expected to facilitate energy dissipation from the nonequilibrium electrons to the substrate.

In spite of its role in limiting the electron mobility in TMDs [15,17], our understanding of heat dissipation through RP scattering remains limited for TMDs. Unlike the phononic TBC which depends on interatomic forces, the RP-mediated electronic TBC (G_{el}) is expected to vary with the electron density (n), which can be modulated by the gate electrode in a field-effect transistor. Thus, a deeper understanding of this phenomenon may inspire the design of novel devices with gate-tunable thermal properties and perhaps shed light on the distribution of reported experimental TBC values [18–21]. Although earlier theoretical and experimental work on RP heat dissipation in graphene [16,22] indicates that G_{el} is small for the graphene-SiO_2 interface and weakly dependent on the electron density, the different electronic structure in single-layer MoS_2 and WS_2 suggests that these findings for graphene may not apply to TMDs.

In our paper, we develop a theoretical model of heat dissipation by RP scattering [16] and apply it to investigate the electronic TBC and its dependence on the electron density, substrate material (SiO_2, HfO_2, and Al_2O_3), and temperature (T) in two commonly studied single-layer TMDs

(MoS$_2$ and WS$_2$). The effects of electron screening on G_{el} are studied. One of our main findings is that the G_{el} for MoS$_2$ and WS$_2$ exhibits a substantially greater dependence on n than the G_{el} for graphene, with G_{el} reaching 85 MW/K/m^2 for the MoS$_2$-Al$_2$O$_3$ interface at the electron density of 10^{13} cm^{-2}. We suggest applications for different substrate materials and how this electron density dependence of the TBC can be exploited to create gate-tunable thermal insulators.

II. THEORETICAL MODEL FOR HEAT DISSIPATION BY REMOTE PHONON SCATTERING

The key elements of our RP model are based on Ref. [16]. We treat the electrons in the TMD as a single-band 2D electron gas (2DEG) at a fixed distance d above the substrate, which we approximate as a dielectric continuum. The treatment of the TMD as a 2D electron gas can be justified by the three-atom thickness of single-layer TMD crystals, which implies that the electrons are strongly confined in the out-of-plane direction. The 2DEG in the TMD has a parabolic dispersion characterized by the effective mass m_e with spin and valley degeneracies g_s and g_v, respectively. For the substrate, the bulk polar optical phonons, of which there are typically two branches for a dielectric insulator such as SiO$_2$, are characterized by their longitudinal optical (LO) and transverse optical (TO) frequencies [12], which are related through the equation $\epsilon_{sub}^0 = \epsilon_{sub}^\infty (\frac{\omega_{LO1}^2}{\omega_{TO1}^2})(\frac{\omega_{LO2}^2}{\omega_{TO2}^2})$, where ϵ_{sub}^0 and ϵ_{sub}^∞ represent, respectively, the static and optical permittivity of the substrate, and ω_{LO1} and ω_{LO2} (ω_{TO1} and ω_{TO2}) are, respectively, the LO (TO) frequencies of the first and second phonon branches with $\omega_{LO1} < \omega_{LO2}$ ($\omega_{TO1} < \omega_{TO2}$). The LO phonon frequencies are determined

from the roots of the frequency-dependent substrate dielectric function

$$\epsilon_{sub}(\omega) = \epsilon_{sub}^\infty + \left(\epsilon_{sub}^i - \epsilon_{sub}^\infty\right)\frac{\omega_{TO2}^2}{\omega^2 - \omega_{TO2}^2}$$
$$+ \left(\epsilon_{sub}^0 - \epsilon_{sub}^i\right)\frac{\omega_{TO1}^2}{\omega^2 - \omega_{TO1}^2}, \qquad (1)$$

where ω and ϵ_{sub}^i are, respectively, the frequency and intermediate permittivity of the substrate. We can rewrite Eq. (1) as $\epsilon_{sub}(\omega) = \epsilon_{sub}^\infty (\frac{\omega_{LO1}^2 - \omega^2}{\omega_{TO1}^2 - \omega^2})(\frac{\omega_{LO2}^2 - \omega^2}{\omega_{TO2}^2 - \omega^2})$. The corresponding surface optical (SO) frequencies associated with the surface electric field, ω_{SO1} and ω_{SO2}, are determined from the solutions to $\epsilon_{sub}(\omega) + \epsilon_0 = 0$ [13]. The electronic TBC is determined from the rate of change of the SO1 and SO2 phonons as they scatter with the electrons in the TMD and the resultant rate of energy dissipation from the electrons, following the approach in Ref. [16].

A. Surface optical phonon emission and absorption rates

From first-order perturbation theory, the rate of change in the Bose-Einstein (BE) occupation factor $N_{\gamma,q}$ of the γ phonon with wave vector q, where $\gamma = $ SO1 and SO2 indexes the SO phonon branch, is [16]

$$\frac{dN_{\gamma,q}}{dt} = -g_s g_v \sum_p \left(W_{\gamma,p \to p+q}^{(abs)} - W_{\gamma,p \to p-q}^{(ems)}\right). \qquad (2)$$

The phonon absorption ($W_{\gamma,p \to p+q}^{(abs)}$) and emission ($W_{\gamma,p \to p-q}^{(ems)}$) terms describe phonon absorption and emission due to the $p \to p+q$ and $p \to p-q$ electronic transitions, respectively, where p is the wave vector of the initial electronic state. The expressions for $W_{\gamma,p \to p+q}^{(abs)}$ and $W_{\gamma,p \to p-q}^{(ems)}$ can be derived from the Fermi golden rule to yield

$$\left\{ \begin{matrix} W_{\gamma,p \to p+q}^{(abs)} \\ W_{\gamma,p \to p-q}^{(ems)} \end{matrix} \right\} = \frac{2\pi |M_{\gamma,q}|^2}{\hbar} \left\{ \begin{matrix} f_p(1 - f_{p+q})N_{\gamma,q}\delta(E_{p+q} - E_p - \hbar\omega_\gamma) \\ f_p(1 - f_{p-q})(N_{\gamma,q} + 1)\delta(E_{p-q} - E_p + \hbar\omega_\gamma) \end{matrix} \right\}, \qquad (3)$$

where $M_{\gamma,q}$ is the electron-phonon coupling coefficient, $f_p = \{\exp[\beta(E_p - \mu)] + 1\}^{-1}$ is the Fermi-Dirac occupation factor for the electronic state p, $N_{\gamma,q}$ is the Bose-Einstein occupation factor $N(\omega_\gamma, T) = [\exp(\beta\hbar\omega_\gamma) - 1]^{-1}$, and $E_p = \hbar^2 p^2/(2m_e)$ and ω_γ represent the electron and phonon energy, respectively. The terms $\beta = (k_B T)^{-1}$ and $\mu = \beta^{-1}\ln[\exp(\frac{2\pi\hbar^2 n\beta}{g_s g_v m_e}) - 1]$ represent, respectively, the inverse temperature and chemical potential, where T is the temperature, n is the electron density, k_B is the Boltzmann constant, and $\hbar$ is the reduced Planck constant.

Given Eq. (3), the sums in Eq. (2) can be written as

$$\sum_p \left\{ \begin{matrix} W_{\gamma,p \to p+q}^{(abs)} \\ W_{\gamma,p \to p-q}^{(ems)} \end{matrix} \right\} = \frac{2\pi\Omega|M_{\gamma,q}|^2}{g_s g_v \hbar} \left\{ \begin{matrix} N_{\gamma,q} S_0(q, \omega_\gamma) \\ (N_{\gamma,q} + 1)S_0(-q, -\omega_\gamma) \end{matrix} \right\},$$

where Ω is the area of the TMD-substrate interface and $S_0(q, \omega)$ is the dynamic structure factor of the 2DEG in the random phase approximation [23], i.e., $S_0(q, \omega) =$

$\frac{g_s g_v}{\Omega} \sum_p f_p(1 - f_{p+q})\delta(E_{p+q} - E_p - \hbar\omega)$, which simplifies to

$$S_0(q, \omega) = \frac{g_s g_v [N(\omega, T) + 1]}{\Omega\pi} \lim_{\eta \to 0^+}$$
$$\times \mathrm{Im} \sum_p \frac{f_{p+q} - f_p}{E_{p+q} - E_p - \hbar\omega + i\eta}$$
$$= \frac{N(\omega, T) + 1}{\pi}\mathrm{Im}\mathcal{P}(q, \omega; \mu, T)$$

and

$$\mathcal{P}(q, \omega; \mu, T) = \frac{g_s g_v}{\Omega} \lim_{\eta \to 0^+} \sum_p \frac{f_{p+q} - f_p}{\hbar\omega - E_{p+q} + E_p + i\eta}. \qquad (4)$$

Equation (4) describes the finite-temperature 2DEG polarizability and can be written as [24]

$$\mathcal{P}(q, \omega; \mu, T_{el}) = \int_0^\infty d\mu' \frac{\mathcal{P}(q, \omega; \mu', 0)}{4k_B T_{el} \cosh^2\left(\frac{\mu - \mu'}{2k_B T_{el}}\right)},$$

where T_{el} is the electronic temperature and, for $z_{\pm} = \hbar\omega \pm \frac{\hbar^2 q^2}{2m_e}$ and $u = \frac{2\mu\hbar^2 q^2}{m_e}$, its exact expression at $T_{el} = 0$ is [24]

$$\mathcal{P}(\boldsymbol{q},\omega;\mu,0) = \frac{g_s g_v m_e}{2\pi\hbar^2} + \frac{g_s g_v m_e^2}{2\pi\hbar^4 q^2}\{\mathrm{sgn}(z_+)\Theta(z_+^2 - u)\sqrt{z_+^2 - u} - \mathrm{sgn}(z_-)\Theta(z_-^2 - u)\sqrt{z_-^2 - u}\}$$

$$+ i\frac{g_s g_v m_e^2}{2\pi\hbar^4 q^2}\{\Theta(u - z_+^2)\sqrt{u - z_+^2} - \Theta(u - z_-^2)\sqrt{u - z_-^2}\}.$$

B. Electron-phonon interaction and screening

The electron-phonon coupling coefficient $M_{\gamma,\boldsymbol{q}}$ in Eq. (3) is [13]

$$M_{\gamma,\boldsymbol{q}} = \left[\frac{e^2\hbar\omega_\gamma \exp(-2qd)}{\Omega q \varepsilon(q)}\left(\frac{1}{\epsilon_{\gamma,\mathrm{hi}}} - \frac{1}{\epsilon_{\gamma,\mathrm{lo}}}\right)\right]^{1/2}, \quad (5)$$

where e is the electron charge. The expressions for $\epsilon_{\mathrm{SO1,hi}}$, $\epsilon_{\mathrm{SO1,lo}}$, $\epsilon_{\mathrm{SO2,hi}}$, and $\epsilon_{\mathrm{SO2,lo}}$ in Eq. (5) are

$$\epsilon_{\mathrm{SO1,hi}} = \frac{1}{2}\left[\epsilon_{\mathrm{sub}}^\infty\left(\frac{\omega_{\mathrm{LO2}}^2 - \omega_{\mathrm{SO1}}^2}{\omega_{\mathrm{TO2}}^2 - \omega_{\mathrm{SO1}}^2}\right) + \epsilon_0\right],$$

$$\epsilon_{\mathrm{SO1,lo}} = \frac{1}{2}\left[\epsilon_{\mathrm{sub}}^\infty\left(\frac{\omega_{\mathrm{LO1}}^2}{\omega_{\mathrm{TO1}}^2}\right)\left(\frac{\omega_{\mathrm{LO2}}^2 - \omega_{\mathrm{SO1}}^2}{\omega_{\mathrm{TO2}}^2 - \omega_{\mathrm{SO1}}^2}\right) + \epsilon_0\right], \quad (6)$$

$$\epsilon_{\mathrm{SO2,hi}} = \frac{1}{2}\left[\epsilon_{\mathrm{sub}}^\infty\left(\frac{\omega_{\mathrm{LO1}}^2 - \omega_{\mathrm{SO2}}^2}{\omega_{\mathrm{TO1}}^2 - \omega_{\mathrm{SO2}}^2}\right) + \epsilon_0\right],$$

$$\epsilon_{\mathrm{SO2,lo}} = \frac{1}{2}\left[\epsilon_{\mathrm{sub}}^\infty\left(\frac{\omega_{\mathrm{LO2}}^2}{\omega_{\mathrm{TO2}}^2}\right)\left(\frac{\omega_{\mathrm{LO1}}^2 - \omega_{\mathrm{SO2}}^2}{\omega_{\mathrm{TO1}}^2 - \omega_{\mathrm{SO2}}^2}\right) + \epsilon_0\right],$$

where ϵ_0 is the permittivity of the vacuum, and the screening function $\varepsilon(q)$ is given by [25]

$$\varepsilon(q)^{-1} = 1 + \frac{e^2\mathrm{Re}\mathcal{P}(\boldsymbol{q},0;\mu,T)}{2\epsilon_0 q}\left[1 - \frac{\epsilon_{\mathrm{sub}}^\infty - \epsilon_0}{\epsilon_{\mathrm{sub}}^\infty + \epsilon_0}\exp(-2qd)\right]. \quad (7)$$

As expected, Eq. (7) becomes $\varepsilon(q)^{-1} = 1 + e^2\mathrm{Re}\mathcal{P}(\boldsymbol{q},0;\mu,T)/(2\epsilon_0 q)$ in the $d \to \infty$ (i.e., no substrate) limit and $\varepsilon(q)^{-1} = 1 + e^2\mathrm{Re}\mathcal{P}(\boldsymbol{q},0;\mu,T)/[(\epsilon_{\mathrm{sub}}^\infty + \epsilon_0)q]$ in the $d = 0$ limit (i.e., no gap between the TMD and substrate). The screening function reduces the bare electron-phonon strength especially in the short wavelength ($q \to \infty$) limit and originates from the polarization of the mobile electrons in the 2DEG to screen the surface electric field generated by the substrate. To obtain the bare electron-phonon strength, we can set $\varepsilon(q)^{-1} = 1$.

C. Electronic thermal boundary conductance

Using the identities $S_0(\boldsymbol{q},\omega) = e^{\beta\hbar\omega}S_0(\boldsymbol{q},-\omega)$ and $S_0(\boldsymbol{q},\omega) = S_0(-\boldsymbol{q},\omega)$, Eq. (2) simplifies to

$$\frac{dN_{\gamma,\boldsymbol{q}}}{dt} = -\frac{2\pi\Omega|M_{\gamma,\boldsymbol{q}}|^2}{\hbar}S_0(\boldsymbol{q},\omega_\gamma)\frac{N_{\gamma,\boldsymbol{q}}(T_{\mathrm{sub}}) - N_{\gamma,\boldsymbol{q}}^{\mathrm{Eq}}}{N_{\gamma,\boldsymbol{q}}^{\mathrm{Eq}} + 1},$$

where $N_{\gamma,\boldsymbol{q}}^{\mathrm{Eq}}$ is the Bose-Einstein occupation factor at the TMD temperature. Given the SO phonon energy density $\varrho(T_{\mathrm{sub}}) = \frac{1}{\Omega}\sum_{\gamma,\boldsymbol{q}}\hbar\omega_\gamma N_{\gamma,\boldsymbol{q}}$, we can write the electronic TBC as the derivative of the rate of change of $\varrho(T_{\mathrm{sub}})$ with respect to T_{sub},

i.e.,

$$G_{\mathrm{el}} = -\frac{d}{dT_{\mathrm{sub}}}\left[\frac{d\varrho(T_{\mathrm{sub}})}{dt}\right]_{T_{\mathrm{sub}}=T}$$

$$= \sum_{\gamma,\boldsymbol{q}}\frac{2\pi\hbar\omega_\gamma^2}{k_B T^2}|M_{\gamma,\boldsymbol{q}}|^2 S_0(\boldsymbol{q},\omega_\gamma)N_{\gamma,\boldsymbol{q}}^{\mathrm{Eq}}.$$

Hence, the final expression for G_{el} is

$$G_{\mathrm{el}} = \sum_{\gamma,\boldsymbol{q}}\frac{2\hbar\omega_\gamma^2}{k_B T^2}|M_{\gamma,\boldsymbol{q}}|^2\left(N_{\gamma,\boldsymbol{q}}^{\mathrm{Eq}} + 1\right)N_{\gamma,\boldsymbol{q}}^{\mathrm{Eq}}\mathrm{Im}\mathcal{P}(\boldsymbol{q},\omega_\gamma;\mu,T),$$

$$(8)$$

which, for the ease of numerical evaluation, we can rewrite as a multivariable integral,

$$G_{\mathrm{el}} = \sum_{\gamma=\mathrm{SO1,SO2}}\mathcal{F}_\gamma\int_0^{q_{\mathrm{max}}}dq\,\frac{\exp(-2qd)}{\varepsilon(q)}$$

$$\times \int_0^\infty d\mu'\frac{\mathrm{Im}\mathcal{P}(\boldsymbol{q},\omega_\gamma;\mu',0)}{4k_B T\cosh^2\left(\frac{\mu-\mu'}{2k_B T}\right)}, \quad (9)$$

where q_{max} is the maximum wave vector, which we can set as $q_{\mathrm{max}} = 2\pi/\sqrt{A} \approx 2 \times 10^{10}$ m^{-1} (A is the unit cell area of the TMD), and

$$\mathcal{F}_\gamma = \frac{e^2\hbar^2\omega_\gamma^3}{\pi k_B T^2}\left(N_\gamma^{\mathrm{Eq}} + 1\right)N_\gamma^{\mathrm{Eq}}\left(\frac{1}{\epsilon_{\gamma,\mathrm{hi}}} - \frac{1}{\epsilon_{\gamma,\mathrm{lo}}}\right). \quad (10)$$

We use the simulation parameters from Table I in our calculations. The TMD-substrate gap size d is a parameter in

TABLE I. Remote phonon scattering simulation parameters for WS$_2$ and MoS$_2$ [26]. The effective electron masses are expressed in terms of the free-electron mass m_0 and taken from Ref. [26]. The parameters $\epsilon_{\mathrm{sub}}^\infty$, $\epsilon_{\mathrm{sub}}^i$, $\epsilon_{\mathrm{sub}}^0$, ω_{TO1}, and ω_{TO2} are taken from Ref. [27].

Substrate	SiO$_2$	Al$_2$O$_3$	HfO$_2$
m_e/m_0	0.31 (WS$_2$) and 0.51 (MoS$_2$)		
g_s	2 (WS$_2$ and MoS$_2$)		
g_v	2 (WS$_2$ and MoS$_2$)		
d (nm)	0.3 (WS$_2$ and MoS$_2$)		
$\epsilon_{\mathrm{sub}}^\infty/\epsilon_0$	2.50	3.20	5.03
$\epsilon_{\mathrm{sub}}^i/\epsilon_0$	3.05	7.27	6.58
$\epsilon_{\mathrm{sub}}^0/\epsilon_0$	3.90	12.53	22.00
ω_{TO1} (meV)	55.60	48.18	12.40
ω_{TO2} (meV)	138.10	71.41	48.35
ω_{SO1} (meV)	60.99	56.08	21.26
ω_{SO2} (meV)	148.97	110.11	55.08

a continuum model in which we treat the substrate as a continuous dielectric solid with a well-defined surface at which the dielectric function changes discontinuously from $\epsilon_{sub}(\omega)$ to ϵ_0. However, there is no well-defined, exact point in atomistic models where we can say that the dielectric function changes suddenly. Hence, the precise value of d cannot be determined from atomistic models. Moreover, the value of d estimated from atomistic models can vary with the chemical configuration of the substrate surface. Thus, given the uncertainty in d, we look at the range of G_{el} values for different values of d, instead of computing G_{el} for a single fixed d value.

We estimate $d = 0.3$ nm for the TMD-SiO$_2$ interfaces from the position of the highest substrate atom to the lowest TMD atom in the TMD-SiO$_2$ supercells optimized with density functional theory (DFT) calculations, the details of which are given in the Appendix. We also assume $d = 0.3$ nm for the TMD-HfO$_2$ and TMD-Al$_2$O$_3$ interfaces, for convenience. Our calculations are repeated for $d = 0$ and $d = 0.6$ nm because of the strong d dependence from the e^{-2qd} term in Eq. (9), to set the upper and lower bounds for G_{el}, respectively.

III. NUMERICAL RESULTS AND DISCUSSION

To understand the experimental implications of the physics underlying the electronic TBC, we compute the electronic TBC G_{el} using Eq. (9) for the single-layer TMDs (MoS$_2$ and WS$_2$) and dielectric substrates (SiO$_2$, Al$_2$O$_3$, and HfO$_2$) at different temperatures (T) and electron densities (n) since T and n can be varied in experiments. In field-effect transistors, the electron density is modulated by the gate electrode and can reach up to $n \sim 10^{13}$ cm^{-2} [15,17]. Intuitively, we expect G_{el} to increase with n as more electron-phonon scattering events occur at higher n. However, at higher n, the mobile electrons can also be polarized by an external electric field and generate a polarization field that attenuates the original external field. This effect is known as screening and it is expected to weaken the effective electron-phonon interaction, possibly offsetting the gain in G_{el} from the greater frequency of electron-phonon scattering. By studying the n dependence of G_{el}, we clarify these two competing effects on G_{el}.

A. G_{el} dependence on electron screening

It is shown in Ref. [16] that G_{el} in single-layer graphene can vary substantially depending on the form of the electron-phonon interaction $M_{\gamma,q}$ in Eq. (5), with G_{el} for the bare or unscreened electron-phonon interaction (i.e., the unscreened G_{el}) up to two orders of magnitude larger than G_{el} for the weaker screened electron-phonon interaction (i.e., the screened G_{el}). Experimental TBC data from Koh and coworkers for the graphene-SiO$_2$ interface [22] suggest that changes in the TBC are only weakly dependent on the electron density n, consistent with the screened $M_{\gamma,q}$. On the other hand, theories involving unscreened remote phonon interaction have been used to model heat dissipation in carbon nanotubes [28]. To settle this question for TMDs and to determine the significance of screening for G_{el} in TMDs, we compute the unscreened and screened G_{el} using Eq. (9). For screened interactions, we use Eq. (7), while for unscreened interactions, we set $\varepsilon(q)^{-1} = 1$ in Eq. (9).
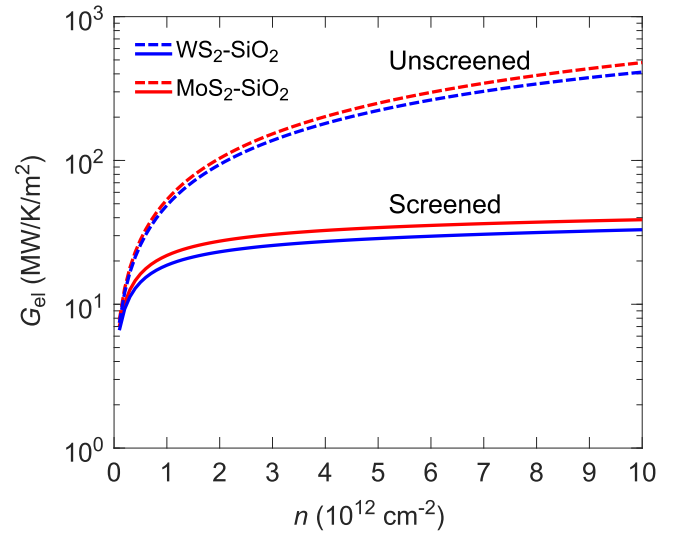

FIG. 1. Electron density dependence of G_{el} for the WS$_2$-SiO$_2$ (blue lines) and MoS$_2$-SiO$_2$ (red lines) interfaces with screened (solid lines) and unscreened (dashed lines) interaction at $T = 300$ K.

Figure 1 shows G_{el} as a function of n at $T = 300$ K for the MoS$_2$-SiO$_2$ and WS$_2$-SiO$_2$ interfaces. For the MoS$_2$-SiO$_2$ interface, the unscreened G_{el} shows an order of magnitude rise from 53 to 479 MW/K/m^2 as n increases from 10^{12} to 10^{13} cm^{-2}, while the screened G_{el} increases from 22 to 39 MW/K/m^2. This difference in the dependence on n illustrates the significance of screening for the TBC. At low n where screening is weak, the unscreened and screened G_{el} values are close, but at high n, the screening of $M_{\gamma,q}$ becomes more significant and the screened G_{el} diverges from the unscreened G_{el}. We surmise that the large unscreened G_{el} increase is unlikely to be correct given the much smaller MoS$_2$-SiO$_2$ TBC observed in Refs. [19,20]. Thus, electron screening must be taken into consideration in order to model electronic heat transfer at TMD-substrate interfaces. Nonetheless, even with the effects of screening, the n dependence of G_{el} is still significant and should be detectable in a MoS$_2$ or WS$_2$ field-effect transistor on a typical Si/SiO$_2$ substrate.

We observe that G_{el} is larger for MoS$_2$ than for WS$_2$. At $n = 10^{12}$ cm^{-2}, the unscreened G_{el} is 53 and 49 MW/K/m^2 for the MoS$_2$-SiO$_2$ and WS$_2$-SiO$_2$ interface, respectively [16], i.e., G_{el} is $\sim$10 percent higher for MoS$_2$. This is due to the higher electron density of states for MoS$_2$, which is a constant proportional to the electron effective mass m_e [29] and corresponds to a greater amount of scattering. The relative difference is further enhanced for the screened G_{el}, with the screened G_{el} for MoS$_2$ about $\sim$17% higher, indicating that a higher m_e also leads to weaker screening of the electron-phonon interaction. This is because at a higher density of states, the greater availability of states lowers the chemical potential, which in turn decreases the screening strength. This combined effect of a lower density of states and stronger screening also explains why G_{el} is significantly lower for graphene. At $n = 10^{12}$ cm^{-2}, the unscreened G_{el} is 53 and 15 MW/K/m^2 for the MoS$_2$-SiO$_2$ and graphene-SiO$_2$ interface, respectively [16]. Unlike the 2DEG in MoS$_2$ or WS$_2$, which has a parabolic dispersion ($E \propto k^2$), the 2DEG in
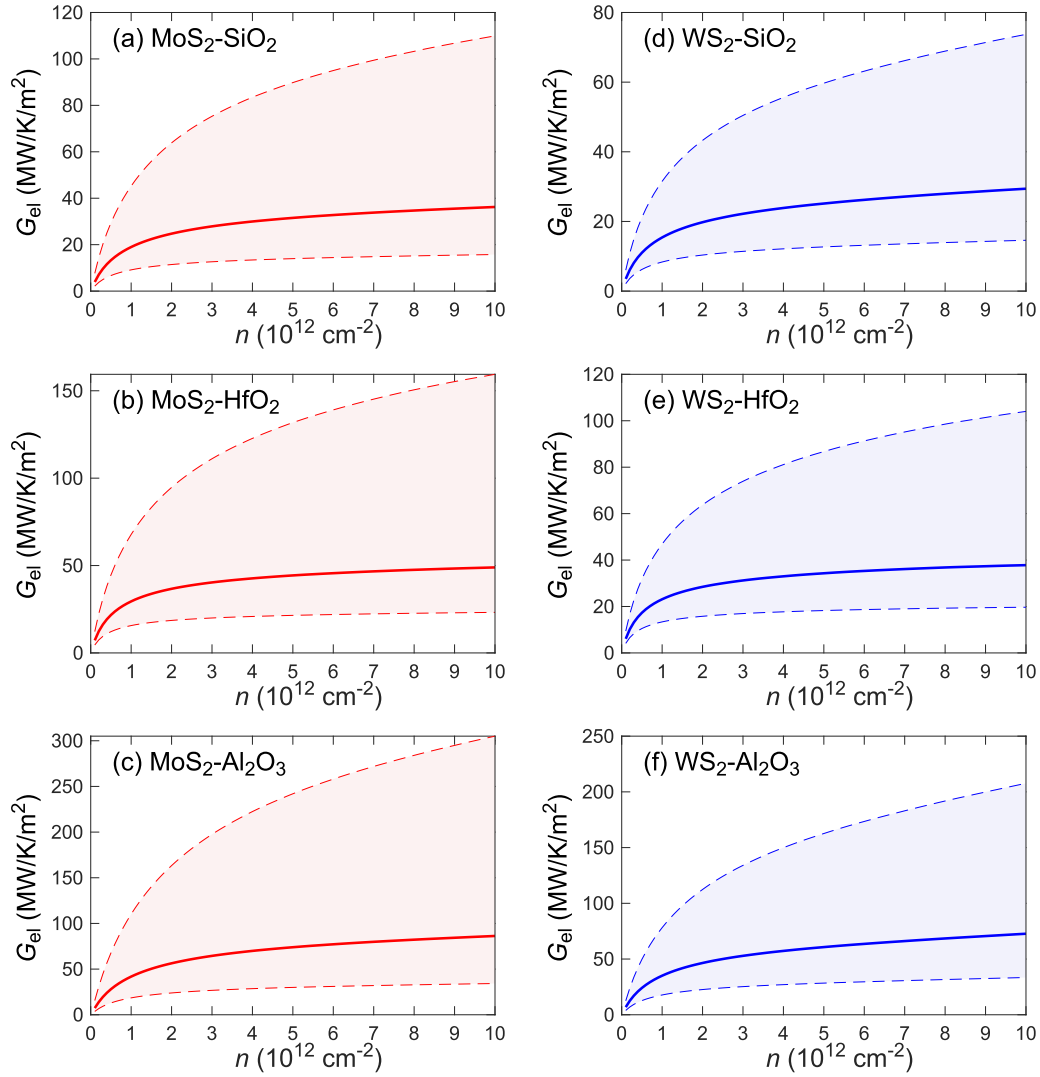
FIG. 2. Electron density dependence of G_{el} for the TMD-substrate interface with different TMDs (WS$_2$ and MoS$_2$) and substrates (SiO$_2$, HfO$_2$, and Al$_2$O$_3$) at $T = 300$ K over the range of $n = 0.1$ to 10×10^{12} cm^{-2} for $d = 0.3$ nm (solid line). The upper and lower bounds in each panel correspond to G_{el} for $d = 0$ and $d = 0.6$ nm (dashed lines).

graphene has a linear dispersion ($E \propto k$) akin to a massless Dirac particle. Thus, the electronic density of states in graphene scales as E near the Dirac point, which results in a reduced amount of scattering and stronger screening of the electron-phonon coupling, leading to a smaller G_{el}.

B. G_{el} dependence on substrate dielectric material, electron density, and temperature

Figures 2(a) to 2(f) show the electronic TBC from Eq. (9) as a function of the electron density n at $T = 300$ K for different substrates (SiO$_2$, HfO$_2$, and Al$_2$O$_3$) and a TMD-substrate distance of $d = 0.3$ nm. The lower and upper bounds for G_{el}, corresponding to $d = 0.6$ and 0.0 nm, respectively, are also shown. As noted earlier, G_{el} increases monotonically from 0 with n because of the higher rate of inelastic scattering events at higher n. However, the rate of increase of G_{el} with respect to n decreases at higher electron densities because the higher rate of inelastic scattering events is offset partially by the greater

electron screening which weakens the electron-phonon coupling. We find that G_{el} is higher for MoS$_2$ than WS$_2$ with every substrate, and that Al$_2$O$_3$ is the substrate with the highest G_{el} because it has the highest bare electron-phonon coupling strength which we can characterize by the dimensionless parameter $\mathcal{C} = \epsilon_0/\epsilon_{sub}^0 - \epsilon_0/\epsilon_{sub}^\infty$ ($\mathcal{C} = 0.147, 0.153,$ and 0.233 for SiO$_2$, HfO$_2$, and Al$_2$O$_3$, respectively). The higher G_{el} for MoS$_2$ can be explained by its greater electron effective mass which is proportional to the electron density of states [29].

By increasing the electron density to $n = 10^{13}$ cm^{-2}, which can be attained in MoS$_2$ field-effect transistors [15,17], G_{el} can reach a maximum of 85, 48, and 39 MW/K/m^2 in Al$_2$O$_3$, HfO$_2$, and SiO$_2$, respectively. This figure represents the gate-tunable component of the overall TBC, which is the sum of G_{el} and G_{ph}, the phononic TBC component, and suggests that the gate-tunable G_{el} is most pronounced and easily observed for the TMD-Al$_2$O$_3$ interface at room temperature since $G_{el} \gg G_{ph}$, as theoretical results from Ref. [30] estimate that $G_{ph} < 4$ MW/K/m^2 for the TMD-Al$_2$O$_3$ interface. This

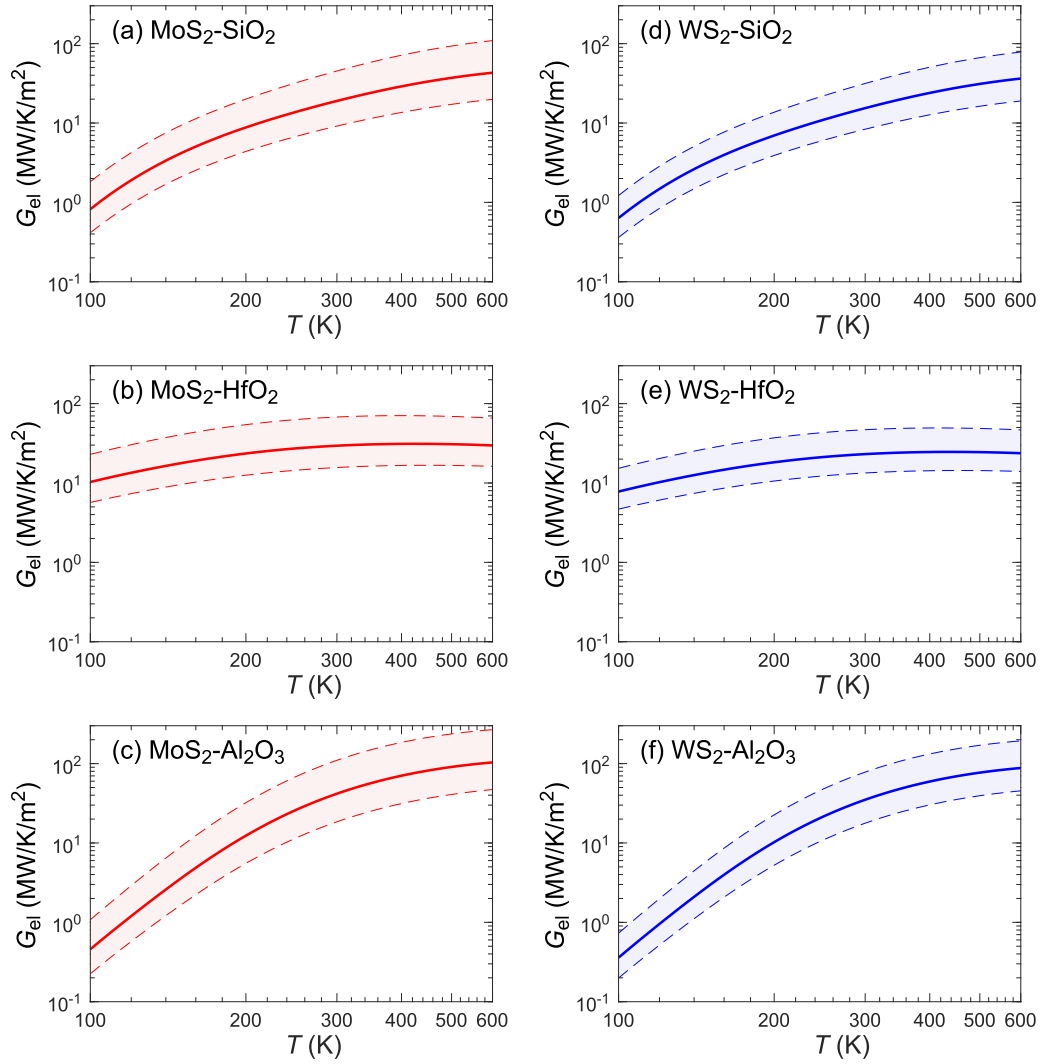FIG. 3. Temperature dependence of G_{el} for the TMD-substrate interface with different TMDs (WS_2 and MoS_2) and substrates (SiO_2, HfO_2, and Al_2O_3) at $n = 10^{12}$ cm^{-2} over the range of $T = 100$ to 600 K for $d = 0.3$ nm. The upper and lower bounds in each panel correspond to G_{el} for $d = 0$ and $d = 0.6$ nm.

tunability should also be observable for the commonly used SiO_2-supported TMD field-effect transistors because classical MD simulation results for the TBC of the MoS_2-SiO_2 interface (15.6 MW/K/m^2 in Ref. [21], 12.2–23.5 MW/K/m^2 in Ref. [31], and 25.6 ± 3.3 MW/K/m^2 in Ref. [6]) suggest that G_{ph} should be in the 10 to 25 MW/K/m^2 range at room temperature for the TMD-SiO_2 interface, comparable to the change in G_{el} from 0 to 39 MW/K/m^2 when n increases from 0 to 10^{12} cm^{-2}. The tunability of G_{el} also suggests that the gate voltage can be adjusted to modulate cross-plane heat transfer between the TMD and the substrate. One can exploit this effect to create gate-tunable thermal insulators by layering the TMD with other 2D materials [32] and then using a gate metal electrode to either raise or lower the TBC to facilitate or inhibit heat transfer at the TMD-substrate interface.

Figures 3(a) to 3(f) show the temperature dependence of G_{el} at $n = 10^{12}$ cm^{-2} for $d = 0.3$ nm from $T = 100$ to 600 K, a temperature range that is experimentally accessible. We find that G_{el} increases monotonically with T in this temperature range for the TMD-SiO_2 and TMD-Al_2O_3 interfaces because

the phonon population increases with T. On the other hand, G_{el} for the TMD-HfO_2 interface exhibits a similar trend (i.e., $dG_{el}/dT > 0$) initially, but plateaus and then starts to decrease with the temperature at higher T because the expression in Eq. (10) scales as $\sim N_\gamma^{Eq}/T^2 \propto 1/T$ at higher T (i.e., $k_B T \gg \hbar\omega_{SO1}$) given the relatively small SO1 phonon frequency ($\omega_{SO1} = 21.26$ meV) in HfO_2. This difference in the behavior of the temperature dependence of G_{el} for different substrates can be used to distinguish the effects of the electronic TBC. With Al_2O_3 as the substrate, we predict that the TBC contribution from G_{el} is not only large (relative to the other substrates), but is expected to have a pronounced temperature dependence that can be verified in experiments, while with HfO_2, the temperature dependence is predicted to be significantly weaker. The distinct temperature dependence of HfO_2 and Al_2O_3 suggests that different substrate materials can be used for heat-transfer applications at different temperature regimes. HfO_2 can be used at low temperatures ($T < 200$ K), while Al_2O_3 can be used at higher temperatures ($T > 300$ K).

IV. SUMMARY AND CONCLUSION

In this work, we have developed a theoretical model of electronic thermal boundary conductance (TBC) via the remote phonon scattering of electrons in single-layer MoS_2 and WS_2 supported on dielectric substrates. We have verified that screened electron-phonon interactions are necessary for realistic predictions. Our model predicts that the electronic TBC is highly dependent on the electron density and is strongly tunable using the gate electrode in field-effect transistors, with the strongest effect seen for Al_2O_3. We have also identified the temperature dependence of the electronic TBC for each dielectric substrate and the temperature regimes at which each substrate material is more effective in interfacial heat transfer. This strong dependence of the electronic TBC on the electron density can be exploited for the design of novel thermal devices with gate voltage-modulated crossplane heat-dissipative properties.

ACKNOWLEDGMENTS

APPENDIX: ESTIMATION OF TMD-SiO₂ GAP

The gap size (d) of the TMD-SiO_2 interface can be estimated from the distance between the highest substrate atom and the lowest TMD atom. The WS_2-SiO_2 and MoS_2-SiO_2 heterostructures are optimized structurally within the framework of density functional theory (DFT) using the software package VASP [33]. The DFT-D2 method is adopted to simulate the van der Waals interactions across the interface, while the Perdew-Burke-Ernzerhof functional is used as the exchange-correlation functional together with a cutoff energy of 400 eV. The slab models of the heterostructures are constructed with a vacuum layer thicker than 10 Å. For the TMD-SiO_2 interface, the heterostructures are constructed from a 3×3 supercell for the TMD (MoS_2 or WS_2) and a
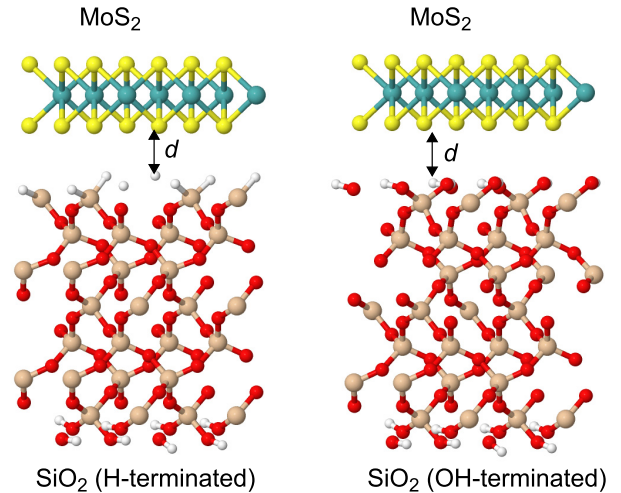

FIG. 4. Side view of the MoS_2-SiO_2 heterostructures used in our density functional theory (DFT) calculations to estimate the gap size d. We obtain $d = 0.253$ nm (H-terminated SiO_2 surface on the left) and 0.306 nm (OH-terminated SiO_2 surface on the right). The Mo, S, H, Si, and O atoms are colored in blue, yellow, white, beige, and red, respectively. The images are generated using JMOL [34].

2×2 supercell for the SiO_2 (001) surface to ensure a better lattice match with lattice strains smaller than 2%. To simulate the SiO_2 substrate, a slab model with seven Si layers is used and the atoms in the bottom O-Si-O atomic layers are saturated with hydrogen atoms and fixed during structural optimization. We adopt a $3 \times 3 \times 1$ Monkhorst-Pack (MP) grid for k-point sampling for the TMD-SiO_2 heterostructures. All the atomic models are fully relaxed until the forces are smaller than 0.005 eV/Å.

Figure 4 shows the MoS_2-SiO_2 heterostructures for different SiO_2 surface configurations (H terminated and OH terminated), similar to those used in Ref. [8]. We estimate $d = 0.253$ and 0.306 nm for the H-terminated and OH-terminated SiO_2 surface, respectively. This shows that the estimate of d can vary with the chemical structure of the substrate surface. Hence, it is simpler to approximate $d = 0.3$ nm for the MoS_2-SiO_2 interface. Our calculations, repeated for the different WS_2-SiO_2 interfacial configurations, such as in Fig. 4, also suggest that $d = 0.3$ nm for the WS_2-SiO_2 interface.

[1] X. Li, L. Yang, M. Si, S. Li, M. Huang, P. Ye, and Y. Wu, Adv. Mater. **27**, 1547 (2015).

[2] D. Lembke, S. Bertolazzi, and A. Kis, Acc. Chem. Res. **48**, 100 (2015).

[3] E. Pop, Nano Res. **3**, 147 (2010).

[4] Z.-Y. Ong and M.-H. Bae, 2D Mater. **6**, 032005 (2019).

[5] Z.-Y. Ong, B. Qiu, S. Xu, X. Ruan, and E. Pop, J. Appl. Phys. **123**, 115107 (2018).

[6] S. V. Suryavanshi, A. J. Gabourie, A. Barati Farimani, and E. Pop, J. Appl. Phys. **126**, 055107 (2019).

[7] B. N. J. Persson, A. I. Volokitin, and H. Ueba, J. Phys.: Condens. Matter **23**, 045009 (2011).

[8] Z.-Y. Ong, Y. Cai, and G. Zhang, Phys. Rev. B **94**, 165427 (2016).

[9] Z.-Y. Ong, Phys. Rev. B **95**, 155309 (2017).

[10] G. C. Correa, C. J. Foss, and Z. Aksamija, Nanotechnology **28**, 135402 (2017).

[11] K. Hess and P. Vogl, Solid State Commun. **30**, 797 (1979).

[12] M. V. Fischetti, D. A. Neumayer, and E. A. Cartier, J. Appl. Phys. **90**, 4587 (2001).

[13] A. Konar, T. Fang, and D. Jena, Phys. Rev. B **82**, 115452 (2010).

[14] K. Zou, X. Hong, D. Keefer, and J. Zhu, Phys. Rev. Lett. **105**, 126601 (2010).

[15] Z. Yu, Z.-Y. Ong, Y. Pan, Y. Cui, R. Xin, Y. Shi, B. Wang, Y. Wu, T. Chen, Y.-W. Zhang, G. Zhang, and X. Wang, Adv. Mater. **28**, 547 (2016).

[16] Z.-Y. Ong, M. V. Fischetti, A. Y. Serov, and E. Pop, Phys. Rev. B **87**, 195404 (2013).

[17] Z. Yu, Y. Pan, Y. Shen, Z. Wang, Z. Y. Ong, T. Xu, R. Xin, L. Pan, B. Wang, L. Sun, J. Wang, G. Zhang, Y. W. Zhang, Y. Shi, and X. Wang, Nat. Commun. **5**, 5290 (2014).

[18] A. Taube, J. Judek, A. Lapinska, and M. Zdrojek, ACS Appl. Mater. Interfaces **7**, 5061 (2015).

[19] E. Yalon, C. J. McClellan, K. K. H. Smithe, M. Munoz Rojo, R. L. Xu, S. V. Suryavanshi, A. J. Gabourie, C. M. Neumann, F. Xiong, A. B. Farimani, and E. Pop, Nano Lett. **17**, 3429 (2017).

[20] E. Yalon, O. B. Aslan, K. K. H. Smithe, C. J. McClellan, S. V. Suryavanshi, F. Xiong, A. Sood, C. M. Neumann, X. Xu, K. E. Goodson, T. F. Heinz, and E. Pop, ACS Appl. Mater. Interfaces **9**, 43013 (2017).

[21] P. Yasaei, C. J. Foss, K. Karis, A. Behranginia, A. I. El-Ghandour, A. Fathizadeh, J. Olivares, A. K. Majee, C. D. Foster, F. Khalili-Araghi, Z. Aksamija, and A. Salehi-Khojin, Adv. Mater. Interfaces **4**, 1700334 (2017).

[22] Y. K. Koh, A. S. Lyons, M. H. Bae, B. Huang, V. E. Dorgan, D. G. Cahill, and E. Pop, Nano Lett. **16**, 6014 (2016).

[23] G. D. Mahan, *Many-Particle Physics* (Springer-Verlag, Boston, 2000).

[24] P. F. Maldague, Surf. Sci. **73**, 296 (1978).

[25] Z.-Y. Ong and M. V. Fischetti, Phys. Rev. B **86**, 121409(R) (2012).

[26] Z. Jin, X. Li, J. T. Mullen, and K. W. Kim, Phys. Rev. B **90**, 045422 (2014).

[27] Z.-Y. Ong and M. V. Fischetti, Phys. Rev. B **86**, 165422 (2012).

[28] S. V. Rotkin, V. Perebeinos, A. G. Petrov, and P. Avouris, Nano Lett. **9**, 1850 (2009).

[29] J. H. Davies, *The Physics of Low-dimensional Semiconductors*, 1st ed. (Cambridge University Press, New York, 1997).

[30] C. J. Foss and Z. Aksamija, 2D Mater. **6**, 025019 (2019).

[31] H. Farahani, A. Rajabpour, M. Khanaki, and A. Reyhani, Comput. Mater. Sci. **142**, 1 (2018).

[32] S. Vaziri, E. Yalon, M. M. Rojo, S. V. Suryavanshi, H. Zhang, C. J. McClellan, C. S. Bailey, K. K. Smithe, A. J. Gabourie, V. Chen, S. Deshmukh, L. Bendersky, A. V. Davydov, and E. Pop, Sci. Adv. **5**, eaax1325 (2019).

[33] G. Kresse and J. Furthmüller, Phys. Rev. B **54**, 11169 (1996).

[34] Created by Jmol: An open-source JAVA viewer for chemical structures in 3D (http://www.jmol.org/).